Biodiesel and fossil-fuel diesel soot oxidation activities of Ag/CeO$_2$ catalyst

Grisel Corro[a,*], Angel Flores[a], Francisico Pacheco-Aguirre[b], Umapada Pal[c], Fortino Bañuelos[a], Araceli Ramirez[d], Alfred Zehe[d]

[a] *Instituto de Ciencias, Benemérita Universidad Autónoma de Puebla, 4 sur 104, 72000 Puebla, Mexico*
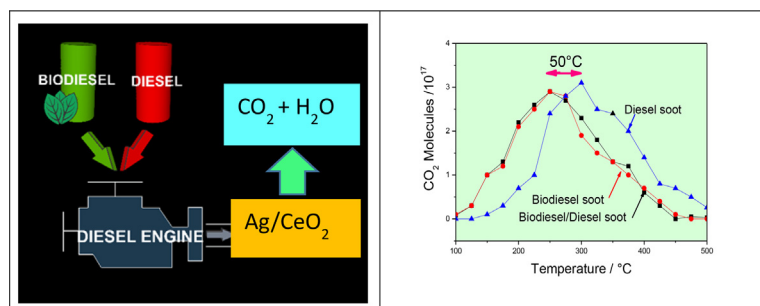[b] *Facultad de Ingeniería Química, Benemérita Universidad Autónoma de Puebla, 4 sur 104, 72000 Puebla, Mexico*
[c] *Instituto de Física, Benemérita Universidad Autónoma de Puebla, Apdo. Postal J-48, 72570 Puebla, Mexico*
[d] *Facultad de Ciencias de la Electrónica, Benemérita Universidad Autonoma de Puebla, 4 sur 104, 72000 Puebla, Mexico*

GRAPHICAL ABSTRACT

ABSTRACT

We present the effects of the addition of biodiesel, derived from waste frying oil, to fossil-fuel diesel, on soot emissions, and on the physicochemical properties of soot particles. Biodiesel was blended with diesel to study the sooting trend of the blended fuel, and the effect of the chemical composition of soot generated from the blended fuel combustion on its reactivity during catalytic oxidation over reduced 3%Ag/CeO$_2$. The emitted soots were characterized by their specific surface areas, SEM, and FTIR, Raman and DRX spectroscopies. The catalyst was characterized by UV–vis optical absorption, XPS and DRX spectroscopy. The composite catalyst showed excellent activity for the oxidation of the soots generated from the combustion of pure diesel, pure biodiesel and diesel-biodiesel blend (50% by volume of each). However, soot generated from pure biodiesel and diesel-biodiesel blend combustion showed higher reactivity for catalyzed oxidation than pure diesel soot. The activity of the catalyst was correlated with the metallic state of Ag at its surface, and with the chemical characteristics of the soot particles generated during the combustion of different fuels. We demonstrate that along with reducing the sooting tendency of diesel, biodiesel addition also leads to soots that are easier to oxidize in particulate filters in diesel engines.

1. Introduction

Diesel, a non-renewable fossil fuel, is of immense importance for on-road transportation, off-road uses, electric power generation, farming marine shipping and so on [1]. However, the major problem associated to the usage of diesel as fuel is the environmental pollution through soot

emission during its combustion [2]. With the depletion of natural reserves of diesel and other fossil fuels, the increase in environmental pollution from emissions during their combustions, and their evergrowing demand due to the rising number of road vehicles, it is essential to develop renewable fuels with lower environmental impact that can be used directly or as blends in conventional engines [3,4].

Biodiesel (methyl ester of fatty acids), obtained from nonedible biomass has proved to be favorable in reducing soot emissions from engines [5–12]. The biodiesel can be produced from various natural sources including waste frying oil [13], jatropha oil, palm oil, neem oil, soybean oil, rapeseed oil and other vegetable oils [14–17]. Biodiesel combustion leads to low CO and unburned hydrocarbon emissions, produces higher combustion efficiency, with higher cetane number, along with lower emissions of sulfur and aromatics than diesel [17–20]. The high viscosity and poor volatility of biodiesel can be overcome by using it in blends with diesel [18,21,22]. While the combustion of B20 (20% biodiesel-80% diesel) blend, produces 0–4% higher NO_x emission with respect to mineral diesel, the production of soot, total unburnt hydrocarbons, and CO emissions are reduced by 10, 20 and 11% respectively [23]. In order to satisfy the emission standards which, become increasingly stringent, even with the use of biodiesel or blended biodiesel, an exhaust gas after treatment system must be used.

Diesel particulate filters (DPFs) can be an effective technology to capture soot particles produced during biodiesel/diesel combustion inside the engines. The DPFs require frequent regeneration through soot oxidation to prevent pressure buildup in the exhaust pipelines, thus a high soot reactivity is desired. Continuous regeneration assisted by the oxidation catalyst is considered to be a more advanced system. In fact, a huge effort has been devoted to develop active soot oxidation catalysts in the last three decades. Several researchers have reported that CeO_2-based oxides possess excellent activity for soot oxidation at the lowest possible temperatures [24–26]. Ag/CeO_2 catalysts have been widely studied recently [27–30]. The reactive phase for soot oxidation over CeO_2 and Ag/CeO_2 has been identified as active oxygen (O_n^{x-}) species [26,31–34]. Machida et al. [31] found that reactive oxygen is formed from gaseous O_2 adsorbed at the three-phase boundary between soot, reduced CeO_2 and the gas phase. However, other active oxygen species, originated from lattice oxygen at the CeO_2 soot interface, also contribute to the total soot oxidation [24,25]. Recently we demonstrated a direct relation between the diesel soot oxidation activities of Ag supported on SiO_2 and ZnO and its electronic state at the catalyst surface [35]. The high activity of Ag/SiO_2 has been attributed to the generation of superoxides by Ag^0 at the SiO_2 surface.

On this basis, in this investigation, we prepared a Ag/CeO_2 catalyst, pretreated in H_2 to increase the probability of silver reduction to its metallic state. The increased Ag^0 sites at the catalyst surface would increase the probability of superoxide generation; thus, should increase the soot oxidation activity of the catalyst. The activity of the catalyst was studied for the oxidation of different soots generated from the combustion of diesel (mineral diesel), biodiesel (produced in our laboratory) and a diesel-biodiesel blend (1/1, v/v). The activities of the catalyst were correlated with the electronic state of Ag at the catalyst surface, and with the chemical characteristics of the soot particles generated during the combustion of different fuels.

2. Material and methods

2.1. Catalysts

CeO_2 powder, supplied by Aldrich (99.99%), was used as support material. The catalyst was prepared through impregnation using the appropriate amount of aqueous $AgNO_3$ (Aldrich 99.99%) solution to obtain nominal $3\%Ag/CeO_2$ mixture. The suspension was magnetically stirred at room temperature for 1 h; after which the catalysts were recovered by filtration and washed thoroughly to remove unreacted species (if any) and dried at 120 °C overnight. After drying, the sample

was reduced under pure H_2 using a feed volume flow rate of 80 ml min^{-1} at 450 °C for 4 h. The temperature of the furnace was increased at the rate of 10 °C min^{-1}. After cooling down to room temperature (25 °C) under H_2 flow, the sample was purged with nitrogen for 30 min and stored in dry conditions, after which it is called $3\%Ag/CeO_2$. A CeO_2 sample, without metal salt solution impregnation was prepared in the same way to use as reference.

A Belsorp (Japan) Mini II sorptometer was used to record the N_2 adsorption-desorption isotherms of the catalysts. Specific surface area (S_g) of the samples was estimated from their N_2 physisorptions at 77 K, using BET analysis. The samples (1 g each) were degassed at 400 °C for 2 h before recording their adsorption-desorption isotherms. After cooling to room temperature (25 °C), the isotherms were recorded in the pressure range 0.0–6.6 kPa. The technique of back extrapolation of the linear portion of the isotherms to zero equilibrium pressure was used to determine the saturation uptake.

X-ray photoelectron spectra (XPS) were recorded on freshly prepared reduced catalysts before and after the different soots oxidation cycles, using an Escalab 200R electron spectrometer equipped with a hemispherical analyzer, operating in a constant pass energy mode. Monochromatic MgK_α emission ($h\nu$ = 1253.6 eV) from the X-ray tube operating at 10 mA and 12 kV was utilized for recording XPS spectra of the samples. Different energy regions of interest of the photoelectrons were scanned a number of times in order to get good signal-to-noise ratios. The intensities of the emission peaks were estimated by determining the integral of each peak after subtracting an S-shaped background and fitting the experimental peak to Lorentzian/Gaussian curves (80%L/20%G). The peak positions of the elements were corrected utilizing the position of C$1s$ peak coming from adventitious carbon appeared at 284.9 ± 0.2 eV.

The diffuse reflectance spectra (DRS) of the catalysts were measured on dry-pressed disks (~15 mm diameter) using a Shimadzu UV–vis spectrophotometer equipped with an integrating sphere, and $BaSO_4$ as standard reflectance sample. The crystallinity and structural phase of the samples were verified through powder X-ray diffraction (XRD), using the CuK_α radiation (λ = 1.5406 Å) of a Bruker D8 Discover diffractometer. The scan range of 10–110° was used with a step size of 0.03° and a scan speed of 10 s/step.

2.2. Characterization of fuels

Mineral diesel used in this investigation was acquired from the Mexican market. This fuel is composed of about 75% saturated hydrocarbons and about 25% aromatic hydrocarbons. It will be designed as B(0) in the present study. The biodiesel used in the present study was prepared in our laboratory from waste frying oil by a two-step catalytic process as described elsewhere [14]. This fuel will be called as B(100). The used diesel-biodiesel blend containing 50% (volume) each, will be designated as B(50). The biodiesel used in this study was characterized for its methyl-esters content by the EN 14103 test method. The determination of the free, bound, and total glycerin, along with mono, di, and triglycerides, was made following the ASTM D 6584 test method.

2.3. Generation of soots

The catalytic activity for soot oxidation could not be determined using commercial black powders (e.g. Printex, Degussa), as the soots of diesel-biodiesel blends are not commercially available. Therefore, we utilized the soots generated in-situ as described in the following section.

The soots of different fuels were generated by burning the fuels in a fuel burner under controlled air flow, as described schematically in Fig. 1. In this study, the term 'soot' is used to refer both the soluble and insoluble (carbon) fractions of the burned fuel-emissions. The emission from the exhaust of the vessel was directed to the catalyst sample (200 mg) placed inside a tubular quartz reactor (inner diameter 10 mm) in a programmable furnace with internally mounted thermocouple
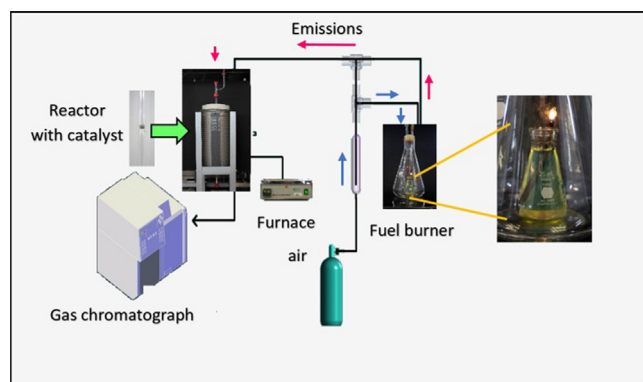
Fig. 1. Schematic diagram of the system used for monitoring the soots combustion catalyzed by 3%Ag/CeO$_2$ process.

(Fig. 1). The precision of the temperature measurement was ± 1 °C. The process was performed using an air feed volume flow rate of 100 cm^3 min^{-1}, consisting of 20% vol. of O$_2$ and 80 %vol. of N$_2$. During the generation of soots, oxygen content in the reaction gas decreased due to the reactions. In order to verify that the combustion of diesel took place in lean conditions, oxygen feed volume flow in the vessel exhaust was monitored by gas chromatography. Oxygen flow remained higher than 10 cm^3 min^{-1} throughout the combustion process (oxygen in excess during diesel combustion). The soot generated from the exhaust of the vessel was accumulated on the catalyst in the tubular reactor.

After 1 h of fuel combustion, the total amount of soot retained by the catalyst in a blank experiment was about 8.45 ± 0.5 mg, (measured using a Shimadzu AX200 balance). The soot/catalyst mass ratio was about 0.042 ± 0.2. The resulting contact between soot and the catalyst in this case was considered as poor contact.

2.4. Soot characterization

Organic functional groups in the soots synthesized in this investigation were analyzed in a Bruker FT-IR spectrometer (Vertex 70) in the 800–4000 cm^{-1} spectral range, with a resolution of 4 cm^{-1}. Thin, uniform KBr pellets prepared with 0.2 wt% of each of the samples were utilized for recording the FT-IR spectra.

Crystallinity of the soot particles was determined through powder X-ray diffraction (XRD), using the same diffractometer used for the analysis of the catalysts. Morphological analysis of the B(0), B(50) and B(100) soots were performed in a JEOL JMS-6610LV scanning electron microscope (SEM) fitted with an OXFORD energy dispersive X-ray spectroscope (EDX), which provided elemental analysis of the samples.

Specific surface area (S$_g$) of the samples and pore size distribution in them were estimated from their N$_2$ physisorptions at 77 K, using BET method. The analysis was performed, with the same sorptometer used for estimating the specific surface area of the catalysts. The samples (~ 0.010 g each) were degassed at 250 °C for 2 h before recording their adsorption-desorption isotherms. After cooling to room temperature (25 °C), the isotherms were recorded in the pressure range 0.0–6.6 kPa. The technique of back extrapolation of the linear portion of the isotherms to zero equilibrium pressure was used to determine the saturation uptake.

Raman spectra of the three diesel soot samples were recorded in the 200–3000 cm^{-1} spectral range in a Horiba, JOBIN-YVON microRaman spectrometer utilizing the 633 nm line (1 mW) of a He-Ne laser as excitation source. The data were collected in backscattered geometry. The laser spot diameter over the samples was about 10 μm, and the spectral resolution of the spectrometer was 3 cm^{-1} at 633 nm. The samples for Raman spectroscopy were prepared by pressing the powder soot samples over glass slides. The intensity ratios of the disordered graphite ('D' band) and graphite ('G' band) peaks were used to determine the

graphitic content in soot samples using a curve-fitting program in OriginLab software. Analysis was made to investigate the short-range order of graphitic-based structure of the soots. As the integrated intensity ratio of disordered graphite ('D' band) to graphite ('G' band) is inversely proportional to microcrystalline planer size, (that corresponds to the in-plane dimension of the single microcrystalline domain in graphite), analysis of spectral features, (such as peak position, intensity, and bandwidth of each of the component bands), was performed to understand the nature of carbonaceous soot samples.

2.5. Soot oxidation through programmed temperature experiments

After the accumulation of soot over the catalyst surface, air was purged for 15 min to remove weakly attached combustion products. The air (20 vol% of O$_2$ and 80 vol% of N$_2$) flow rate was maintained at 100 cm^3·min^{-1}. The mixture was then heated from room temperature (25 °C) to 600 °C at the rate of 5 °C·min^{-1}. A thermocouple was inserted into the soot-catalyst mixture to monitor its temperature along with the exothermic heat of the soot oxidation. The emissions from the reactor were analyzed through a computer programmed Shimadzu gas chromatograph provided with a thermo-conductivity detector (TCD) to monitor the CO$_2$ evolution at different temperatures. The chromatograph was fitted with a Porapak column to analyze CO$_2$ evolutions as a function of the temperature of the soot-catalyst mixture. The process comprising soot accumulation on the catalyst at room temperature (during 1 h), its subsequent oxidation at high temperature, and then cooling down to 25 °C is designated as a cycle. The duration of each cycle was about 5 h. Fig. 2 shows the temperature-time profile of a complete cycle. After the first cycle, five similar cycles were performed over the same catalyst sample.

3. Results and discussion

3.1. Catalysts characterization

3.1.1. Surface area analysis

The specific surface area of the catalysts before and after utilization in oxidation cycles was estimated from their N$_2$ adsorption–desorption isotherms recorded at 77 K. Obtained results revealed a specific surface area of 23 m^2 g^{-1} and 45 m^2 g^{-1} for CeO$_2$ and 3%Ag/CeO$_2$ catalysts respectively.

3.1.2. X-ray diffraction characterization of the catalysts

The XRD spectra of the fresh CeO$_2$, 3%Ag/CeO$_2$ before and after 6 B (0) soot oxidation cycles are shown in Fig. 3. The 3%Ag/CeO$_2$ fresh sample revealed four clear diffraction peaks of metallic Ag (2θ = 38.1°,
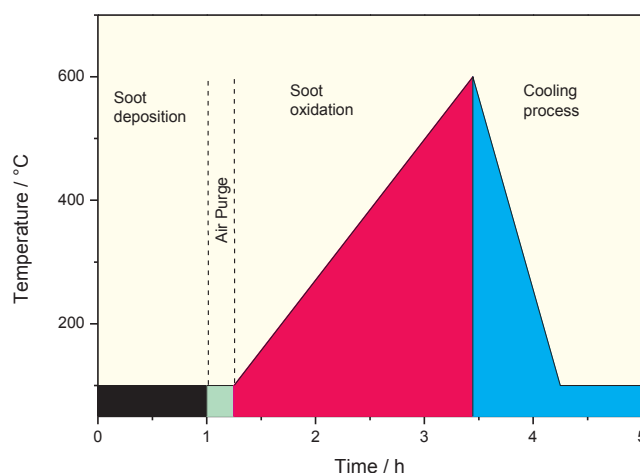

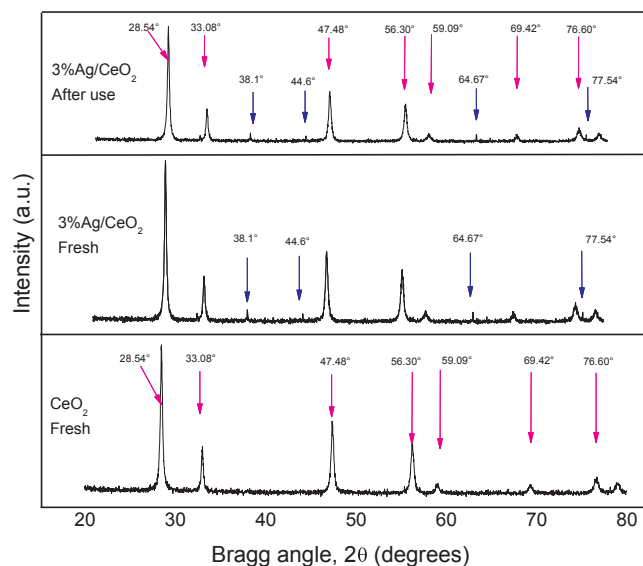**Fig. 2.** Temperature-time profile of a complete soot oxidation cycle.

Fig. 3. XRD patterns of CeO₂ and 3%Ag/CeO₂ before and after 6 B(0) soot oxidation cycles. Pink arrows indicate the locations of CeO₂ diffraction peaks. Blue arrows indicate the diffraction peaks of Ag⁰ in fcc structure. (For interpretation of the references to colour in this figure legend, the reader is referred to the web version of this article.)

44.6°, 64.67°, 77.54°), which could be indexed to face centered cubic (fcc) crystal structures (JCPDS # 87–0717), while no diffraction due to silver oxide was observed. The sharp and intense peaks appeared at 2θ = 28.54°, 33.08°, 47.48°, 56.30°, 59.09°, 69.42°, 76.60°, 79.08°, are the characteristic diffraction peaks of CeO₂ support (JCPDS 43-1002). The spectra of 3%Ag/CeO₂ before and after 6 B(0) soot oxidation cycles revealed the same diffraction peaks of metallic Ag⁰. XRD spectra of 3%Ag/CeO₂ after 6 B(50) and B(100) soot oxidation cycles (not presented) revealed also the same diffraction peaks of metallic Ag⁰. These results indicate that the silver nanoparticles formed at the surface of CeO₂ have high thermal and chemical stability, even in the strong oxidizing conditions during the soot oxidizing cycles.

3.1.3. Diffuse reflectance spectra of the catalysts

Fig. 4 presents the UV–Vis diffuse reflectance spectra (DRS) of the 3%Ag/CeO₂ and CeO₂ samples. The DRS spectrum of CeO₂ revealed a broad absorption band between 200 and 400 nm, and a sharp absorption edge around 380 nm. While a simple extrapolation of the sharp
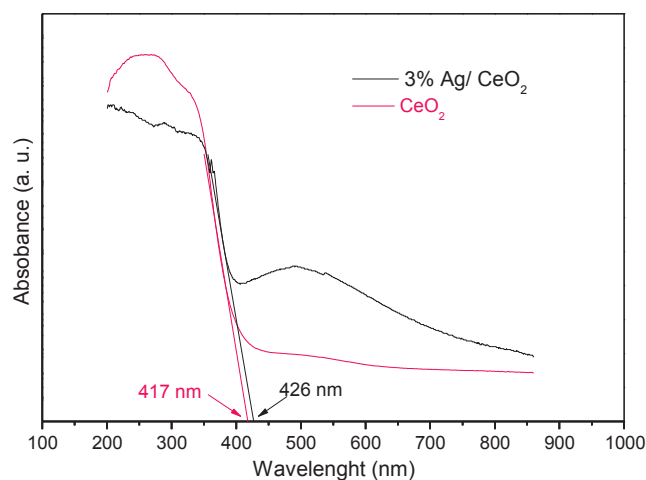

Fig. 4. UV–Vis DRS absorption spectra of CeO₂ and 3%Ag/CeO₂ samples. The band edge position values of the catalysts are indicated by arrows of respective colors.

absorption section revealed a band gap energy of ~2.97 eV for the fresh CeO₂ sample, the broad higher energy absorption band appeared in the sample is probably the result of overlapping of the bands at 267 and 326 nm, associated to the Ce^{3+}-O^{2-} charge transfer and Ce^{4+}-O^{2-} interband transitions [36,37].

On the other hand, the absorption spectrum of 3%Ag/CeO₂ sample revealed two bands. The first band appeared between 400 and 650 nm, with maximum around 500 nm, corresponding to the overlapping of silver surface plasmon resonance (SPR) signal (400–550 nm) with the σ-σ* and n-σ* transition signals of Agₙ clusters, which appear in the 330–360 nm and 440–540 nm spectral range, respectively [38]. The second band is observed with onset at 426 nm, which is close to the absorption edge of CeO₂ showing a band gap value of about 2.87 eV. It is important to note that the band attributed to Ag_4^{2+} [39,40] could not be observed due to the overlapping of broad absorption signals of CeO₂, spreading through 200–400 nm. The reduced absorption in the 220–350 nm spectral range for the 3%Ag/CeO₂ sample compared with the CeO₂ sample is probably due to the formation of a few larger Ag particles over CeO₂, which do not absorb UV light.

3.1.4. XPS characterization of the 3%Ag/CeO₂ catalyst

High resolution XPS spectra of the fresh 3%Ag/CeO₂ catalyst and after B(0) soot, B(50) soot and B(100) soot oxidation cycles are displayed in Fig. 5. The Ag $3d_{5/2}$ emission band in the fresh 3%Ag/CeO₂ sample peaked around 368.0 eV, corresponds to Ag⁰ electronic state [41–43]. The positions of Ag $3d_{5/2}$ emission band from the sample, before and after utilization in soot oxidation cycles are presented in Table 1. As can be seen in the table, the position of Ag $3d_{5/2}$ emission remained almost same even after using the catalysts for 6 cycles of soot oxidation, irrespective of the nature of soot. The result indicates that the zero valent (metallic) electronic state of silver in 3%Ag/CeO₂ remained unaltered even after its use in the oxidation cycles. The XPS estimated Ag/Ce atomic ratios in the catalyst before and after its use in soot oxidation cycles are also presented in Table 1. The Ag/Ce atomic ratio at the surface of the catalyst before and after its use remained almost same. These results suggest that the silver nanoparticles formed at the surface of CeO₂ have high thermal and chemical stability, even in the strong oxidizing conditions during the soot oxidizing cycles.
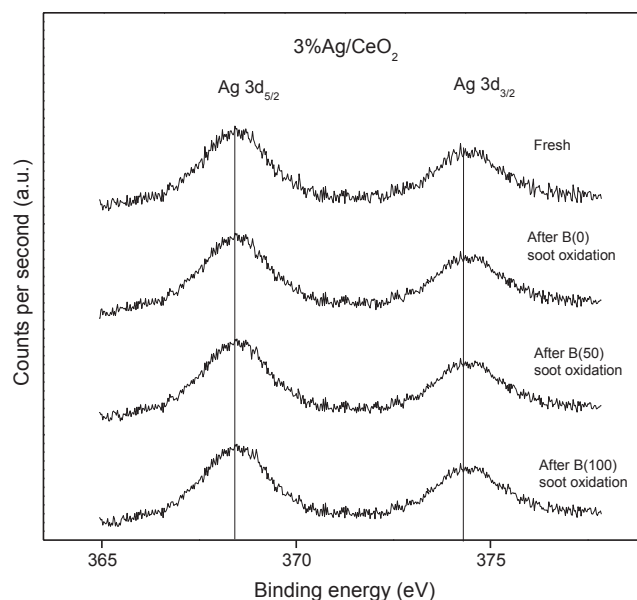

Fig. 5. XPS spectra of 3%Ag/CeO₂: fresh and after 6 B(0), B(50), and B(100) soot oxidation cycles.

Table 1

Binding energy position of the Ag $3d_{5/2}$ emission, and Ag/Ce atomic ratios at the surface of the 3%Ag/CeO$_2$ catalyst, before and after its use in 6 soot oxidation cycles. The % peak areas of Ag $3d_{5/2}$ component in the samples (fresh and used) are presented in parentheses.

Catalyst 3%Ag/CeO$_2$	Soot used for oxidation cycles	Ag $3d_{5/2}$ (eV)		Ag/Ce
Fresh	–	368.12	(100)	0.17
Used	B0 soot	368.01	(100)	0.15
Used	B50 soot	368.13	(100)	0.15
Used	B100 soot	368.08	(100)	0.16

Table 2

Physical and chemical properties of biodiesel used for soot generation.

Property	Units	Value
Density at 15 °C	kg·m^{-3}	870
Kinematic viscosity at 40 °C	mm^2·s^{-1}	4.0
Ester content	% (m·m^{-1})	98.8
Monoglyceride	% (m·m^{-1})	0.01
Diglyceride	% (m·m^{-1})	0.0058
Triglyceride	% (m·m^{-1})	0.0009
Free glycerin	% (m·m^{-1})	0.08

3.2. Characterization of biodiesel used for B(100) soot and B(50) soot generation

The biodiesel used in this study was produced in our laboratory from waste frying oil by a two-step catalytic process, as reported in our previous publication [14]. The qualitative and quantitative analysis of the biodiesel are reported in Table 2. As can be seen in this table, the obtained biodiesel contains 98.8% of methyl-esters, and very low contents of monoglyceride, diglyceride and triglycerides, demonstrating its high quality for practical use.

3.3. Characterization of B(0), B(50), and B(100) soots

3.3.1. Fourier transform infrared spectroscopy

Fig. 6 shows the FT-IR spectra of B(0), B(50), and B(100) soots synthesized in this investigation. The FT-IR spectra of the soots revealed peaks within the mid-infrared region. The bands observed for the three samples indicate that, regardless of the fuel used to generate them, almost all the functional groups were present in the three soots. However, the band observed at 1548 cm^{-1} for the B(0), and B(50) soots, corresponding to C=C stretching of aromatics and alkenes was not
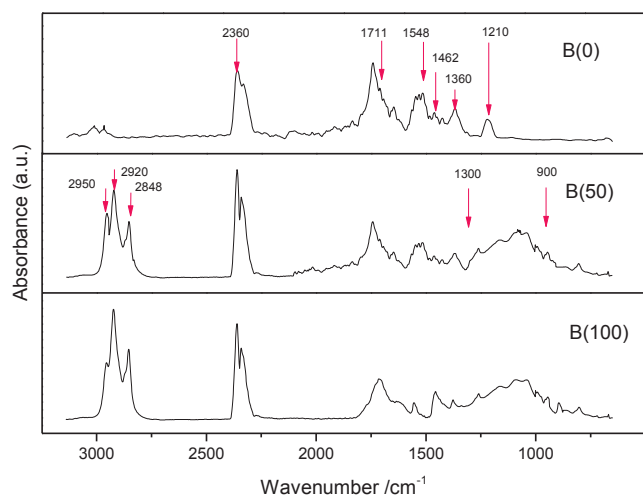

Fig. 6. FT-IR spectra of soots collected from the combustion vessel exhaust during the burning of B(0), B(50), and B(100) samples.

detected in B(100). Moreover, differences in signal intensities were observed for the three soots. The observed differences in the FT-IR spectra of the soots are in well agreement with the chemical composition of their origin. The C—H stretching corresponding to alkane-type and alkene-type functional groups was observed at 2950 cm^{-1}, 2920 cm^{-1} and 2854 cm^{-1}, respectively. The intensities of these peaks were found to decrease from B(100) to B(0), indicating a lower aliphatic hydrocarbon content in B(0).

The peak revealed around 1711 cm^{-1} assigned to the carbonyl C=O stretching in aliphatic and aromatic aldehydes and ketones, was present in all the three soots, indicating that the soots generated from B(0), B(50) and B(00) fuels contain these same compounds. The peak at about 1548 cm^{-1} was assigned to C=C stretching of aromatics and alkenes. The signal at about 1462 cm^{-1} corresponds to conventional coke [44,45]. The signal appeared at 1360 cm^{-1} has been observed in graphite, carbon black and activated carbon [46].

On the other hand, the peaks appeared between 1300 and 900 cm^{-1} were attributed to C—O stretching in ethers, and esters present in the soots [47]. Although the intensities of these peaks were high for B(100) and B(50) soots, they were not detected in B(0) soot; indicating the B(100) soot and B(50) soot are richer in oxygenated functional groups than the B(0) soot. It is interesting to note the appearance of a clear signal at 1210 cm^{-1} in the FT-IR spectrum of B(0) soot. The signal probably corresponds to sulfate compounds formed in the soot particles during the combustion of sulfated compounds present in mineral diesel fuel.

From the results obtained, it can be concluded that the soot produced from B(0) or mineral diesel contains lower amounts of aliphatic carbons and oxygen containing compounds than the soots produced from B(50) and B(100) combustion. The oxygenated groups present in the soots produced from B(50) and B(100) combustion, upon heating, initiate soot oxidation at relatively lower temperatures. Moreover, aliphatic carbons react with oxygen at lower temperatures than aromatic hydrocarbons. Obtained results may also support the higher oxidative reactivity of the soots produced from B(100) and B(50), with respect to the oxidative reactivity of soot produced from B(0), as described in the following section.

3.3.2. SEM analysis

Typical SEM images of the B(0), B(50) and B(100) soots are shown in Supporting Information Section (Fig. S1). The size of the formed soot particles varied between 200 and 500 nm for all the three soots. It is interesting noting that the three soots presented a strong amorphous structure despite the nature of the burned fuel.

3.3.3. Composition analysis of the soots

While the FTIR analysis results qualitatively indicated that B(50) and B(100) had a higher amount of oxygenated functional groups, to obtain a quantitative information on the elemental composition of B(0), B(50), and B(100) soots, their EDX spectra were recorded and analyzed with EDAX Genesis software. The results (Table 3) indicated the presence of C and O atoms in the soots (as H atoms cannot be detected with this technique). Clearly, the addition of biodiesel increases the amounts of oxygenated compounds in the soots. The B(0) soot revealed lowest

Table 3

B(0) soot, B(50) soot and B(100) soot characterization data.

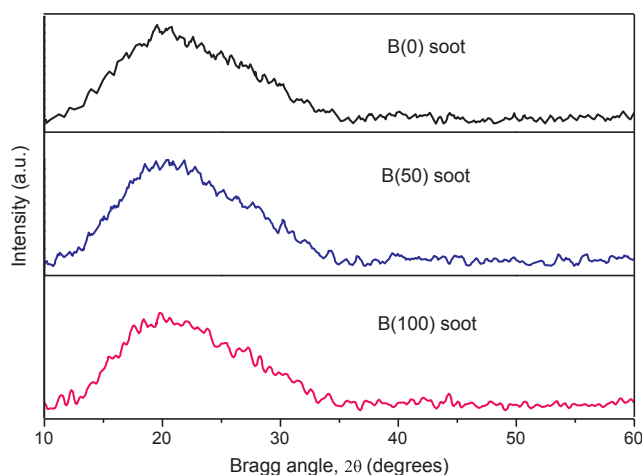| Soot	Specific surface area (m^2 g^{-1})	Total pore volume (cm^3 g^{-1})	Average pore diameter (nm)	Element composition (wt%)		
				C	O	C/O
B(0)	100.57	0.51	20.55	96.06	3.95	24.3
B(50)	77.47	0.44	22.78	94.96	5.04	18.8
B(100)	166.45	0.98	23.75	93.53	6.47	14.4

Fig. 7. X-ray diffraction (XRD) pattern of B(0), B(50), and B(100) soots.

oxygen content (3.95 wt%) and the B(100) soot revealed highest (6.47 wt%) oxygen content.

3.3.4. X-ray diffraction

Fig. 7 shows the XRD spectra of B(0), B(50), and B(100) soots. In the figure, it can be seen a wide signal spreading through 2θ values from 15 to 35°, revealing highly amorphous nature of the three soots.

3.3.5. N_2 adsorption-desorption isotherms of the soots

The influence of the surface area on the oxidation behavior of the soots is expected to provide important insights, because oxygen chemisorption on the active surface sites and the subsequent formation of surface complexes are expected to depend upon the specific surface area of soot particles. The N_2 adsorption-desorption isotherms of all the soots revealed (Fig. S2, Supporting Information) type II adsorption, characteristics of nonporous or little porous solids with meso- and macroporosity. The initial inflation in the adsorption branch below 0.1 relative pressure indicate the completion of monolayer adsorption and start of multilayer adsorption. The BET estimated specific surface area, pore volume and average pore diameter in the three soots are summarized in Table 3. As can be noted, while B(100), presents the highest values of specific surface area, average pore diameter, and total pore volume, it presents the lowest C/O ratio compared with B(0) and B(50) soots. These values indicate a high oxygen chemisorption rate on the B(100) soot particles, thus a higher oxidation activity during combustion. It can also be seen in Table 3 that B(50) soot presents lowest specific surface area compared with B(100) and B(0). The results suggest the growth rate of B(50) soot particles probably increased by the interaction of the different molecules of diesel and biodiesel present in B(50) fuel.

3.3.6. Raman spectroscopy

Fig. 8 presents the Raman spectra acquired for the three diesel soot samples. As can be observed, all the spectra revealed two broad and overlapping bands at intensity maxima ~1592 cm^{-1} and ~1334 cm^{-1}. While the intensity maximum at ~1592 cm^{-1} is known as G band, the intensity maximum at ~1334 cm^{-1} corresponds to disordered graphitic mode or the D band [48].

A detailed analysis of spectral parameters was performed by deconvolution of the experimental Raman profiles. As can be observed in Fig. S3 (Supporting Information), Raman spectra of all the samples could be deconvoluted in four component bands: the graphitic band G around 1600 cm^{-1}, the D1 band peaked around 1340 cm^{-1} associated to disorder graphite, the D3 band around 1530 cm^{-1} associated to amorphous carbon fraction in the sample, and D4 band in-between 1200 and 1235 cm^{-1} associated to disordered graphitic lattice due to
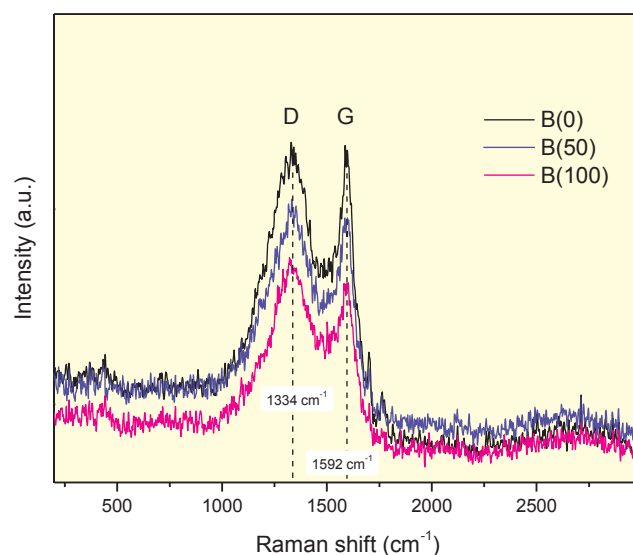

Fig. 8. Raman spectra of the diesel soots generated by the combustion of fossil fuel diesel (B0), mixture of fossil fuel diesel and biodiesel (B50) and biodiesel (B100).

polyenes and/or ionic impurities. In Table S1 it can be noticed that the full width at half maximum (FWHM) of the G band is narrower than that of the D band for all the soots, indicating that the G peak corresponds mostly to a crystalline phase of carbon with nanocrystalline particles.

Table S1 also presents the detailed curve fitted data along with the ratio of graphite to disorder graphite content (G/(D1 + D3 + D4)) in the soot samples. As can be noticed, the graphitic to non-graphitic fraction (ratio) in the fossil fuel diesel soot is higher than the soots extracted from blended and pure biodiesels, indicating the fossil fuel diesel soot contains the smallest fraction of disordered graphitic phases among the three soot samples [49].

3.4. Soot oxidation over the catalysts

The oxidation of different soots over the catalysts in 25–600 °C temperature range are represented in Figs. 9–12. The results of CO_2 evolution as a function of oxidation temperature presented in the figures are summarized in Table 4. In this table, the temperatures at which the soot oxidation started, the soot oxidation reached its maximum, and
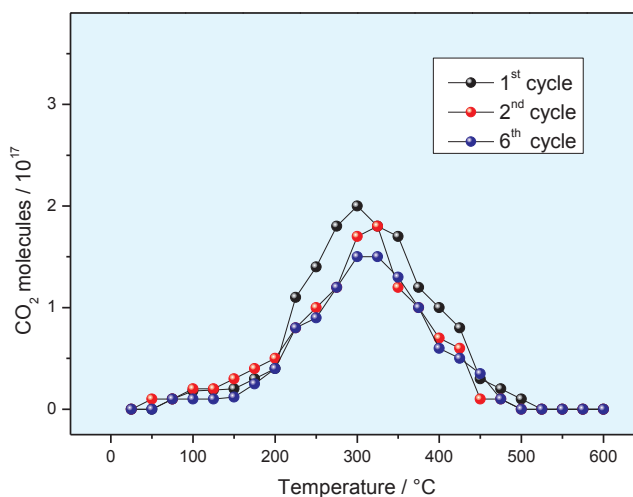

Fig. 9. Evolution of CO_2 as a function of temperature during B(0) soot oxidation over CeO_2.
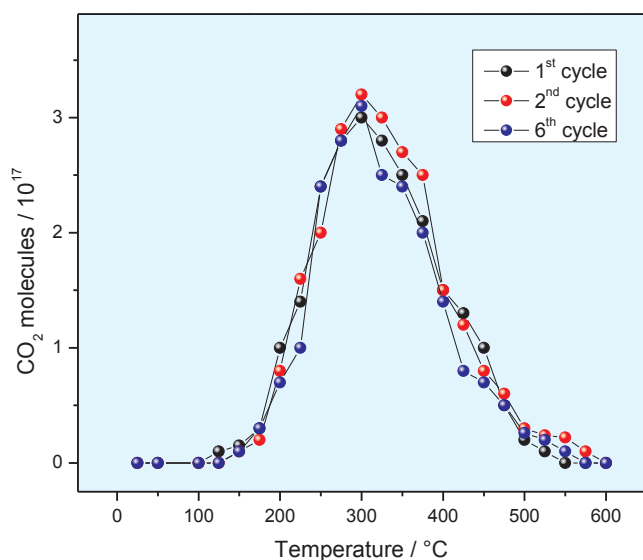
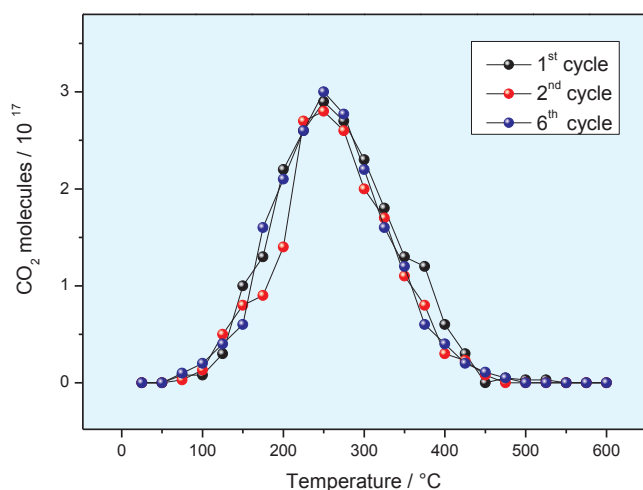**Fig. 10.** Evolution of CO_2 as a function of temperature during B(0) soot oxidation over $3\%Ag/CeO_2$.

Fig. 11. Evolution of CO_2 with temperature during B(50) soot oxidation over $3\%Ag/CeO_2$.

Fig. 12. Evolution of CO_2 as a function of temperature during B(100) soot oxidation over $3\%Ag/CeO_2$.

Table 4
Temperatures at which the oxidation started ($T_{Initial}$); temperatures when the oxidation reached a maximum (T_{Max}) and temperatures when the reaction completed (T_{Final}) for the catalysts during the first cycle of the different soots oxidation.

Catalyst	B(X) soot	Temperatures (°C)		
		$T_{Initial}$	T_{Max}	T_{Final}
CeO_2	B(0) soot	175	325	475
	B(50) soot	150	275	475
	B(100) soot	150	275	450
$3\%Ag/CeO_2$	B(0) soot	150	300	475
	B(50) soot	125	250	450
	B(100) soot	125	250	425

soot oxidation completed during the first oxidation cycle, over the catalysts are designated as ($T_{Initial}$), (T_{Max}), and (T_{Final}), respectively.

3.4.1. CeO_2

Fig. 9 shows the B(0) soot oxidation features over CeO_2 between 25 and 600 °C. There appeared a broad CO_2 evolution signal between 150 and 450 °C during the first B(0) soot oxidation cycle. However, this signal decreased during the subsequent reaction cycles, indicating a slow and continuous catalyst deactivation during the oxidation cycles.

In Table S2, integrated areas under CO_2 evolution for CeO_2 during the oxidations of B(0) soot, B(50) soot and the B(100) soot are reported. As can be noticed, the amounts of CO_2 generated during the oxidation cycles decreased from cycle to cycle for all the soots. These results indicate that CeO_2 reduced in pure hydrogen at high temperature presents a low stability and low activity for soot oxidation, irrespective of the nature of the soot.

3.4.2. $3\%Ag/CeO_2$

Fig. 10 shows the temperature evolution of CO_2 during B(0) soot oxidation over $3\%Ag/CeO_2$ catalyst during 6 soot oxidation cycles.

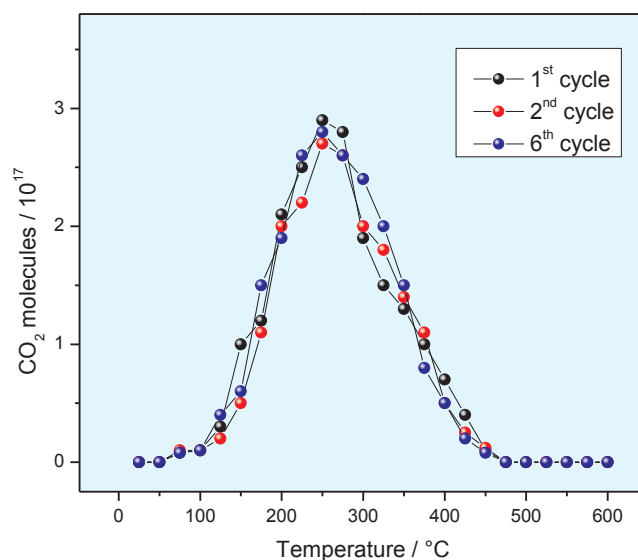In all the 6 evolution curves, there appeared a broad signal through

150–450 °C peaking at about 300 °C, indicating that the highest B(0) oxidation temperature (T_{Max}) remains the same for all the cycles. In Table S2, the areas integrated under CO_2 evolution for $3\%Ag/CeO_2$ during the oxidations of B(0) soot are reported. It can be seen that the amounts of CO_2 generated during the different soot oxidation cycles remained rather fixed from cycle to cycle. These results indicate a strong stability of the catalyst in soot oxidation reaction.

Figs. 11 and 12 present the evolution of CO_2 as a function of the temperature of B(50) soot oxidation and of B(100) soot oxidation respectively, over $3\%Ag/CeO_2$ catalyst during 6 soot oxidation cycles. Similar to the oxidation of B(0) soot, there appeared broad CO_2 oxidation signals in the 150–400 °C range for the oxidations of B(50) soot and the B(100) soot catalyzed over $3\%Ag/CeO_2$.

The areas integrated under CO_2 evolution for the catalyst during the oxidations of B(0) soot, B(50) soot and the B(100) soot reported in Table S2 show that the amounts of CO_2 generated during B(0) soot oxidation are slightly higher than the amounts of CO_2 generated during the oxidations of B(50) and B(100) soots. The result indicates that addition of biodiesel to common mineral diesel is advantageous as it produces lower amount of soot while burning.

It is very interesting to note that for $3\%Ag/CeO_2$, the T_{Max} for both the B(50) soot and B(100) soot oxidation curves is around 250 °C, which is about 50 °C lower than the same for B(0) soot oxidation. As can be noticed further in Figs. 11 and 12, and in Table 4, the T_{Max} of B(50) soot and B(100) soot oxidation remained unchanged from cycle to cycle, until the sixth cycle as for the oxidation of soot produced from B(0). Moreover, the areas integrated under CO_2 evolution for the catalyst

during the oxidations of B(0) soot, B(50) soot and the B(100) soot (Table S2), (i.e. the amounts of CO_2 generated during the oxidation of different soots), did not change from cycle to cycle. These results suggest that during the oxidation cycles of the three different soots, the stoichiometry and electronic structure of the catalyst remained the same. This assumption is supported by the XRD and XPS results, which revealed that the metallic electronic state of silver (Ag^0) in the catalyst surface remained the same even after the six B(0) soot, B(50) soot and B(100) soot oxidation cycles. The unaltered electronic state of Ag^0 and the unaltered activity of the catalyst during the different soot oxidation cycles suggest that metallic Ag^0 is the active species for the reaction. It is important to note that the catalyst operates at temperatures of diesel engine exhaust gas (< 400 °C).

On the other hand, the results presented in Figs. 10–12 and in Table 4 indicate that the T_{Max} for the B(50) soot oxidation and B(100) soot oxidation curves is about 50 °C lower than for that of for the B(0) soot oxidation. The difference of T_{Max} values presented by 3%Ag/CeO$_2$ for the oxidation of the different soots can neither be explained by electronic change of the catalyst during the reactions. The XRD and XPS results presented in Table 1 and Figs. 3–5 show that 3%Ag/CeO$_2$ catalyst remained electronically and morphologically unaltered after the oxidation of different soots.

Now, the FT-IR spectra of the different soots indicated clear differences in their chemical composition. These spectra demonstrated the presence of higher amounts of the very reactive aliphatic and oxygenated groups in B(100) soot and B(50) soot compared with B(0) soot. The aliphatic and oxygenated groups present in B(100) and B(50) soots may have been oxidized at relatively low temperature, and the huge exothermic heat generated during their oxidation might have been transferred to other molecules needing higher activation energies for oxidation, resulting in a low temperature soot combustion. In the case of B(0) soot oxidation, which contains lower amounts of aliphatic and oxygenated groups, the exothermic heat transfer to other molecules needing higher activation energies for oxidation is probably low, and therefore, higher temperatures will be needed to attain their activation, resulting in higher temperature for soot combustion. These results are confirmed by the EDX analysis, which revealed a lower C/O ratio composition on B(100) and B(50) soots than on B(0) soot. On the other hand, the analysis of the structural properties of the different soots, using Raman spectroscopy, revealed that B(100) and B(50) soots have higher amorphous character than B(0) soot. This fact indicates a less ordered structure that has smaller size layers and more defective layers, leading to an increase in the ratio of the number of edge carbon atoms to those in the basal plane of the soot particles, resulting in higher oxidation reactivity, thus in a lower soot combustion temperature [2,50].

Based on the results revealed in Raman spectra of the diesel soots, the similar T_{Max} values for the B(50) soot oxidation and B(100) soot oxidation curves (Figs. 11 and 12 and Table 4) can be explained considering the similar amorphous character of both the B(50) and B(100) soots. Moreover, the similar reactivities of the B(50) and B(100) soots, as indicated by their similar T_{Max} values, might be closely related to their similar chemical composition as revealed by their FTIR spectra.

The activity of 3%Ag/CeO$_2$ catalyst has been compared with the activity of 3%Ag/SiO$_2$ and 3%Ag/ZnO, which were studied recently for B(0) soot oxidation [35]. These catalysts were prepared in our laboratory in the same conditions as 3%Ag/CeO$_2$. For the three catalysts, soot deposition and soot oxidation conditions were the same as the ones described in the present investigation [35]. Fig. 13 presents the evolution of CO_2 as a function of temperature for B(0) soot oxidation (6th cycle), over each catalyst. In Table S3, integrated areas under CO_2 evolution (A_{CO2}) for the three catalysts during the 6th oxidation cycle of B(0) soot are reported.

In Fig. 13 and Table S3, it can be noticed that while 3%Ag/ZnO generated low amounts of CO_2, thus, presented relatively low activity for B(0) soot oxidation [35], 3%Ag/SiO$_2$ generated higher amounts of
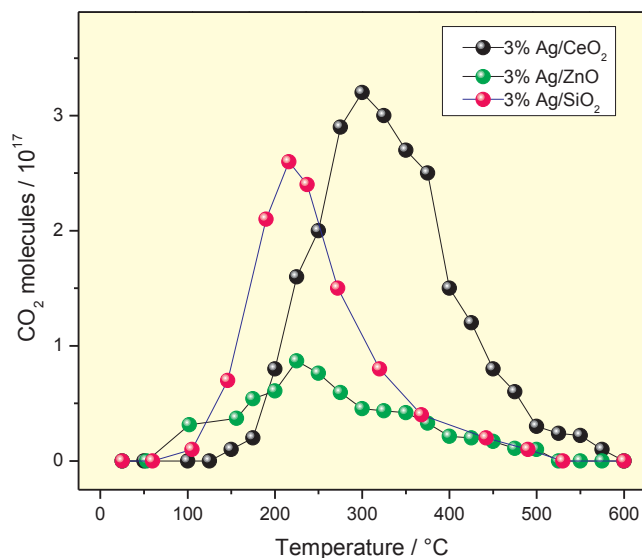

Fig. 13. Evolution of CO_2 as a function of temperature during B(0) soot oxidation over 3%Ag/CeO$_2$, 3%Ag/ZnO [35], and 3%Ag/SiO$_2$ [35].

CO_2 indicating higher activity for the reaction [35]. Now, 3%Ag/CeO$_2$, generated the highest amounts of CO_2 compared with the other two catalysts. These results may indicate that 3%Ag/CeO$_2$ retains and oxidizes higher amounts of soot emissions from the fuel burner compared with 3%Ag/ZnO or 3%Ag/SiO$_2$.

Alternatively, the generation of CO_2 in different amounts during the B(0) soot oxidation over the three catalysts can be explained considering the differences in selectivity of the catalysts towards CO_2 or CO generation. Fig. S4 shows the evolution of CO as a function of temperature in B(0) soot oxidation (6th cycle) over the catalysts. Very low amounts of CO were detected in the temperature range studied over the three catalysts. In Table S3, the ratio of the intensity of CO_2 evolution (A_{CO2}) and the intensity of CO evolution (A_{CO}) is presented. This ratio can be understood as the selectivity of the catalyst in the generation of CO_2 and CO. It can be noticed that 3%Ag/CeO$_2$ presents the highest selectivity to CO_2 generation supporting the conclusion that this catalyst retains and oxidizes higher amounts of soot emitted from the fuel burner in comparison with 3%Ag/ZnO and 3%Ag/SiO$_2$ catalysts. In earlier investigations [26–34], diesel soot oxidation activity of silver supported metal oxide catalysts has been attributed to the generation of superoxides by metallic Ag^0 at their surface. However, recently we demonstrated that while 3%Ag/ZnO presents very low amounts of metallic Ag^0 species at its surface, and is not so active for diesel soot oxidation, 3%Ag/SiO$_2$ contains higher amounts of Ag^0 at its surface and presents higher activity for soot oxidation. Now, the highest activity of 3%Ag/CeO$_2$ for soot oxidation can be related to the high amount of metallic Ag^0 at its surface. Notwithstanding, other active oxygen species, originated from lattice oxygen at the CeO$_2$ soot interface, might also contribute to the total soot oxidation as it has been demonstrated earlier [24,25].

The blending of biodiesel with diesel, enriched soot generated during their combustion with oxygenated functional groups, aliphatic compounds and amorphous character, probably results in an increase in soot reactivity during its catalytic oxidation over 3%Ag/CeO$_2$. Thus, along with the reduced sooting tendency of diesel (mineral), addition of biodiesel for its blending, is not only helpful for economy, but also leads to soots that are easier to oxidize in particulate filters containing suitable catalyst such as 3%Ag/CeO$_2$ in diesel motors.

4. Conclusions

The blending of biodiesel with diesel, resulted in a decrease of the

amount of soot emissions from diesel combustion. Addition of biodiesel to diesel modifies the nature of soot particles emanating from burning the resulting fuel, which contain higher amounts of aliphatic and oxygenated compounds, which are very reactive for further catalytic oxidation over 3%Ag/CeO$_2$ at relatively lower temperature. The high activity presented by this catalyst for the B(0) soot, B(50) soot and B(100) soot oxidation, is probably due to the presence of metallic Ag^0 species at its surface, as revealed by XPS analysis. The presence of Ag^0 species at the surface of the composite catalyst generates during oxidation reactions, high amounts of O$_2^-$ which are very active species for improving soot oxidation. Results presented in this study suggest that the addition of biodiesel to diesel and the use of reduced 3%Ag/CeO$_2$ in particulate filters in diesel engines can lead to a substantial reduction of soot particle emissions from diesel engines, and contribute to improve environment conditions.

Acknowledgements

Appendix A. Supplementary data

Supplementary data to this article can be found online at https://doi.org/10.1016/j.fuel.2019.03.043.

References

[1] Bacha J, Freel J, Gibbs A, Gibbs L, Hemighaus G, Hoekman K, et al. Diesel fuels technical review. California: Chevron Global Marketing; 2007. https://www.chevron.com/-/media/chevron/operations/documents/diesel-fuel-tech-review.pdf.

[2] Omidvarborna H, Kumar A, Kim D-S. Recent studies on soot modeling for diesel combustion. Renew Sustain Energy Rev 2015;48:635–47. https://doi.org/10.1016/j.rser.2015.04.019.

[3] Dincer I. Renewable energy and sustainable development: a crucial review. Renew Sustain Energy Rev 2000;4:157–75. https://doi.org/10.1016/S1364-0321(99)00011-8.

[4] Murugesan A, Umarani C, Subramanian R, Nedunchezhian N. Bio-diesel as an alternative fuel for diesel engines: a review. Renew Sustain Energy Rev 2009;13:653–62. https://doi.org/10.1016/j.rser.2007.10.007.

[5] Kulkarni MG, Dalai AK. Waste Cooking oil an economical source for biodiesel: a review. Ind Eng Chem Res 2006;45(9):2901–13. https://doi.org/10.1021/ie0510526.

[6] Lapuerta M, Rodríguez-Fernández J, Oliva F, Canoira L. Biodiesel from Low-grade animal fats: diesel engine performance and emissions. Energy Fuels 2009;23(1):121–9. https://doi.org/10.1021/ef800481q.

[7] Mofijur M, Atabani AE, Masjuki HH, Kalam MA, Masum BM. A study on the effects of promising edible and non-edible biodiesel feedstocks on engine performance and emissions production: a comparative evaluation. Renew Sustain Energy Rev 2013;23:391–404. https://doi.org/10.1016/j.rser.2013.03.009.

[8] Rizwanul Fattah IM, Masjuki HH, Liaquat AM, Ramli R, Kalam MA, Riazuddin VN. Impact of various biodiesel fuels obtained from edible and non-edible oils on engine exhaust gas and noise emissions. Renew Sustain Energy Rev 2013;18:552–67. https://doi.org/10.1016/j.rser.2012.10.036.

[9] Sevigné Itoiz E, Fuentes-Grünewald C, Gasol CM, Garcés E, Alacid E, Rossi S, et al. Energy balance and environmental impact analysis of marine microalgal biomass production for biodiesel generation in a photobioreactor pilot plant. Biomass Bioenergy 2012;39:324–35. https://doi.org/10.1016/j.biombioe.2012.01.026.

[10] Haldar SK, Ghosh BB, Nag A. Studies on the comparison of performance and emission characteristics of a diesel engine using three degummed non-edible vegetable oils. Biomass Bioenergy 2009;33(8):1013–8. https://doi.org/10.1016/j.biombioe.2008.01.021.

[11] Brosowski A, Thrän D, Mantau U, Mahro B, Erdmann G, Adler P, et al. A review of biomass potential and current utilisation – status quo for93 biogenic wastes and residues in Germany. Biomass Bioenergy 2016;95:257–72. https://doi.org/10.1016/j.biombioe.2016.10.017.

[12] Umar MS, Jennings P, Urmee T. Generating renewable energy from oil palm biomass in Malaysia: the Feed-in Tariff policy framework. Biomass Bioenergy 2014;62:37–46. https://doi.org/10.1016/j.biombioe.2014.01.020.

[13] Corro G, Tellez N, Bañuelos F, Mendoza ME. Biodiesel from Jatropha curcas oil using Zn for esterification step and solar radiation as energy source. Fuel 2012;97:72–9. https://doi.org/10.1016/j.fuel.2012.02.029.

[14] Corro G, Tellez N, Jimenez T, Tapia A, Banuelos F, Vazquez-Cuchillo O. Biodiesel from waste frying oil. Two step process using acidified SiO$_2$ for esterification step.

[15] Karmakar A, Karmakar S, Mukherjee S. Properties of various plants and animals feedstocks for biodiesel production. Bioresour Technol 2010;101(19):7201–10. https://doi.org/10.1016/j.biortech.2010.04.079.

[16] Demirbas A. Progress and recent trends in biodiesel fuels. Energy Convers Manage 2009;50(1):14–34. https://doi.org/10.1016/j.enconman.2008.09.001.

[17] Singh SP, Singh D. Biodiesel production through the use of different sources and characterization of oils and their esters as the substitute of diesel: a review. Renew Sustain Energy Rev 2010;14(1):200–16. https://doi.org/10.1016/j.rser.2009.07.017.

[18] Ashraful AM, Masjuki HH, Kalam MA. Particulate matter, carbon emissions and elemental compositions from a diesel engine exhaust fueled with diesel-biodiesel blends. Atmos Environ 2015;120:463–74. https://doi.org/10.1016/j.atmosenv.2015.09.028.

[19] Canakci M. Combustion characteristics of a turbocharged DI compression ignition engine fueled with petroleum diesel fuels and biodiesel. Bioresour Technol 2007;98(6):1167–75. https://doi.org/10.1016/j.biortech.2006.05.024.

[20] Buyukkaya E. Effects of biodiesel on a DI diesel engine performance, emission and combustion characteristics. Fuel 2010;89(10):3099–105. https://doi.org/10.1016/j.fuel.2010.05.034.

[21] Ali OM, Mamat R, Abdullah NR, Abdullah AA. Analysis of blended fuel properties and engine performance with palm biodiesel–diesel blended fuel. Renewable Energy 2016;86:59–67. https://doi.org/10.1016/j.renene.2015.07.103.

[22] Dhar A, Kevin R, Agarwal AK. Production of biodiesel from high-FFA neem oil and its performance, emission and combustion characterization in a single cylinder DICI engine. Fuel Process Technol 2012;97:118–29. https://doi.org/10.1016/j.fuproc.2012.01.012.

[23] Hess MA, Haas MJ, Foglia TA. Attempts to reduce NOx exhaust emissions by using reformulated biodiesel. Fuel Process Technol 2007;88(7):693–9. https://doi.org/10.1016/j.fuproc.2007.02.001.

[24] Aneggi E, de Leitenburg C, Dolcetti G, Trovarelli A. Promotional effect of rare earths and transition metals in the combustion of diesel soot over CeO$_2$ and CeO$_2$–ZrO$_2$. Catal Today 2006;114(1):40–7. https://doi.org/10.1016/j.cattod.2006.02.008.

[25] Setiabudi A, Chen J, Mul G, Makkee M, Moulijn JA. CeO$_2$ catalysed soot oxidation: the role of active oxygen to accelerate the oxidation conversion. Appl Catal B 2004;51(1):9–19. https://doi.org/10.1016/j.apcatb.2004.01.005.

[26] Krishna K, Bueno-López A, Makkee M, Moulijn JA. Potential rare earth modified CeO$_2$ catalysts for soot oxidation: I. Characterisation and catalytic activity with O2. Appl Catal B 2007;75(3):189–200. https://doi.org/10.1016/j.apcatb.2007.04.010.

[27] Luches P, Pagliuc F, Valeri S, Illas F, Preda G, Pacchioni G. Nature of Ag islands and nanoparticles on the CeO$_2$ (111) surface. J Phys Chem C 2012;116:1122–32. https://doi.org/10.1021/jp210241c.

[28] Hu S, Wang W, Wang Y, Xu Q, Zhu J. Interaction of Zr with CeO$_2$(111) thin film and its influence on supported Ag nanoparticles. J Phys Chem C 2015;119:18257–66. https://doi.org/10.1021/acs.jpcc.5b04325.

[29] Kayama T, Yamasaki K, Shinjoh H. Nanostructured ceria-silver synthesized in a one pot redox reaction catalyzes carbon oxidation. J Am Chem Soc 2010;132:13154–455. https://doi.org/10.1021/ja105403x.

[30] Aneggi E, Llorca J, de Leitenburg C, Dolcetti G, Trovarelli A. Soot combustión over silver-supported catalysts. Appl Catal B 2009;91:489–98. https://doi.org/10.1016/j.apcatb.2009.06.019.

[31] Machida M, Murata Y, Kishikawa K, Zhang D, Ikeue K. On the reasons for high activity of CeO2 catalyst for soot oxidation. Chem Mater 2008;20(13):4489–94. https://doi.org/10.1021/cm800832w.

[32] Shimizu K-i, Kawachi H, Satsuma A. Study of active sites and mechanism for soot oxidation by silver-loaded ceria catalyst. Appl Catal B 2010;96(1):169–75. https://doi.org/10.1016/j.apcatb.2010.02.016.

[33] Yamazaki K, Kayama T, Dong F, Shinjoh H. A mechanistic study on soot oxidation over CeO2–Ag catalyst with 'rice-ball' morphology. J Catal 2011;282(2):289–98. https://doi.org/10.1016/j.jcat.2011.07.001.

[34] Yamazaki K, Sakakibara Y, Dong F, Shinjoh H. The remote oxidation of soot separated by ash deposits via silver–ceria composite catalysts. Appl Catal A 2014;476:113–20. https://doi.org/10.1016/j.apcata.2014.02.014.

[35] Corro G, Vidal E, Cebada S, Pal U, Bañuelos F, Vargas D, et al. Electronic state of silver in Ag/SiO$_2$ and Ag/ZnO catalysts and its effect on diesel particulate matter oxidation: an XPS study. Appl Catal B 2017;216:1–10. https://doi.org/10.1016/j.apcatb.2017.05.059.

[36] Bensalem A, Muller JC, Bozon-Verduraz F. Faraday communications. From bulk CeO2 to supported cerium–oxygen clusters: a diffuse reflectance approach. J Chem Soc, Faraday Trans 1992;88(1):153–4.

[37] Zaki MI, Hussein GAM, Mansour SAA, Ismail HM, Mekhemer GAH. Ceria on silica and alumina catalysts: dispersion and surface acid-base properties as probed by X-ray diffractometry, UV-Vis diffuse reflectance and in situ IR absorption studies. Colloids Surf A 1997;127(1):47–56. https://doi.org/10.1016/S0927-7757(96)03943-X.

[38] Mitchell SA, Kenney-Wallace GA, Ozin GA. Disilver: spectroscopy and photoprocesses in rare-gas matrixes. J Am Chem Soc 1981;103(20):6030–5. https://doi.org/10.1021/ja00410a007.

[39] Linnert T, Mulvaney P, Henglein A, Weller H. Long-lived nonmetallic silver clusters in aqueous solution: preparation and photolysis. J Am Chem Soc 1990;112(12):4657–64. https://doi.org/10.1021/ja00168a005.

[40] Ershov BG, Janata E, Henglein A, Fojtik A. Silver atoms and clusters in aqueous solution: absorption spectra and the particle growth in the absence of stabilizing Ag + ions. J Phys Chem 1993;97(18):4589–94. https://doi.org/10.1021/j100120a006.

[41] Richter M, Langpape M, Kolf S, Grubert G, Eckelt R, Radnik J, et al. Combinatorial

preparation and high-throughput catalytic tests of multi-component deNOx catalysts. Appl Catal B 2002;36(4):261–77. https://doi.org/10.1016/S0926-3373(01)00290-9.

[42] Hoflund GB, Hazos ZF, Salaita GN. Surface characterization study of Ag, AgO, and Ag₂O using x-ray photoelectron spectroscopy and electron energy-loss spectroscopy. Phys Rev B 2000;62(16):11126–33. https://doi.org/10.1103/PhysRevB.62.11126.

[43] She X, Flytzani-Stephanopoulos M. The role of AgOAl species in silver–alumina catalysts for the selective catalytic reduction of NOx with methane. J Catal 2006;237(1):79–93. https://doi.org/10.1016/j.jcat.2005.09.036.

[44] Salamanca M, Mondragón F, Agudelo JR, Benjumea P, Santamaría A. Variations in the chemical composition and morphology of soot induced by the unsaturation degree of biodiesel and a biodiesel blend. Combust Flame 2012;159(3):1100–8. https://doi.org/10.1016/j.combustflame.2011.10.011.

[45] Bellamy LJ. The infrared spectra of complex molecules. London: Chapman and Hall; 1975. https://doi.org/10.1007/978-94-011-6017-9.

[46] Sarbak Z. Characterization and infrared study of the effect of Cr, Mo and W on carbon deposition on platinum/alumina. Appl Catal A 1999;177(1):85–97. https://doi.org/10.1016/S0926-860X(98)00249-X.

[47] Stuart B. Infrared spectroscopy: fundamentals and applications. Hoboken, NJ: John Wiley & Sons, Ltd; 2005. https://doi.org/10.1002/0470011149.

[48] Patel M, Azanaza Ricardo CL, Scardi P, Aswath PB. Morphology, structure and chemistry of extracted diesel soot—Part I: Transmission electron microscopy, Raman spectroscopy, X-ray photoelectron spectroscopy and synchrotron X-ray diffraction study. Tribol Int 2012;52:29–39. https://doi.org/10.1016/j.triboint.2012.03.004.

[49] Sharma V, Uy D, Gangopadhyay A, O'Neill A, Paxton WA, Sammut A, et al. Structure and chemistry of crankcase and exhaust soot extracted from diesel engines. Carbon 2016;103:327–38. https://doi.org/10.1016/j.carbon.2016.03.024.

[50] Omidvarborna H, Kumar A, Kim DS. Variation of diesel soot characteristics by different types and blends of biodiesel in a laboratory combustion chamber. Sci Total Environ 2016;544:450–9.